

Fast Subpixel Mapping Algorithms for Subpixel Resolution Change Detection

Qunming Wang, Peter M. Atkinson, and Wenzhong Shi

Abstract—Due to rapid changes on the Earth's surface, it is important to perform land cover change detection (CD) at a fine spatial and fine temporal resolution. However, remote sensing images with both fine spatial and temporal resolutions are commonly not available or, where available, may be expensive to obtain. This paper attempts to achieve fine spatial and temporal resolution land cover CD with a new computer technology based on subpixel mapping (SPM): The fine spatial resolution land cover maps (FRMs) are first predicted through SPM of the coarse spatial but fine temporal resolution images, and then, subpixel resolution CD is performed by comparison of class labels in the SPM results. For the first time, five fast SPM algorithms, including bilinear interpolation, bicubic interpolation, subpixel/pixel spatial attraction model, Kriging, and radial basis function interpolation methods, are proposed for subpixel resolution CD. The auxiliary information from the known FRM on one date is incorporated in SPM of coarse images on other dates to increase the CD accuracy. Based on the five fast SPM algorithms and the availability of the FRM, subpixels for each class are predicted by comparison of the estimated soft class values at the target fine spatial resolution and borrowing information from the FRM. Experiments demonstrate the feasibility of the five SPM algorithms using FRM in subpixel resolution CD. They are fast methods to achieve subpixel resolution CD.

Index Terms—Change detection (CD), remote sensing, subpixel mapping (SPM), superresolution mapping.

NOMENCLATURE

CD	Change detection.
FRM	Fine spatial resolution land cover map.
HC	Pixel-based hard classification.
MERIS	Medium Resolution Imaging Spectrometer.
MODIS	Moderate Resolution Imaging Spectroradiometer.
OA	Overall accuracy.
PSA	Pixel swapping algorithm.
RBF	Radial basis function.
SPM	Subpixel mapping.

Manuscript received December 13, 2013; revised March 14, 2014, May 8, 2014, and July 2, 2014; accepted August 1, 2014. This work was supported in part by the Research Grants Council of Hong Kong under Grant PolyU 5249/12E, by the Ministry of Science and Technology of China under Grant 2012BAJ15B04 and Project 2012AA12A305, and by the National Natural Science Foundation of China under Grant 41331175. (Corresponding author: Wenzhong Shi.)

Q. Wang is with the Department of Land Surveying and Geo-Informatics, The Hong Kong Polytechnic University, Kowloon, Hong Kong (e-mail: wqm11111@126.com).

P. M. Atkinson is with Geography and Environment, University of Southampton, Southampton SO17 1BJ, U.K. (e-mail: P.M.Atkinson@soton.ac.uk).

W. Shi is with the Joint Research Laboratory on Spatial Information, The Hong Kong Polytechnic University, Kowloon, Hong Kong, and also with Wuhan University, Wuhan 430072, China (e-mail: lswzshi@polyu.edu.hk).

Color versions of one or more of the figures in this paper are available online at <http://ieeexplore.ieee.org>.

Digital Object Identifier 10.1109/TGRS.2014.2346535

SPSAM	Subpixel/pixel spatial attraction model.
STARFM	Spatial and temporal adaptive reflectance fusion model.
STHSPM	Soft-then-hard SPM.
UOC	Class allocation method that allocates classes for subpixels in units of classes.

I. INTRODUCTION

CHANGE detection (CD) in remote sensing is a process in which multitemporal datasets are used to analyze and quantify temporal changes in Earth surface properties [1], [2]. Since remote sensing data can cover the same scene periodically and the digital format is suitable for further computer processing, they are a major source of information for CD. As one of the most important objectives in remote sensing, CD is applied in ecosystem monitoring, damage assessment, disaster monitoring, urban expansion, planning, and land management [1]. Further details of CD applications using remote sensing technologies and existing CD methods can be found in reviews in [1]–[5].

With increasing change on the Earth's surface (particularly due to land cover, in highly developed areas, and as a function of changes in climate), timely CD is becoming increasingly important. Sensors such as the MODIS can cover the same area on a daily basis and have been in operation for over ten years. However, a problem is that MODIS provides images with coarse spatial resolutions only, ranging from 250 to 1000 m. It is usually desirable to monitor changes at a fine spatial resolution to provide as much detailed information as possible. There is always a tradeoff between spatial resolution and temporal resolution. For example, although the Landsat sensors can provide remote sensing images at a finer spatial resolution (30 m) than MODIS, it can only revisit the same area every 16 days. Note that some satellites are able to capture fine spatial resolution images with relatively short revisit time (on a daily basis), such as WorldView and GeoEye, but the high budget and narrow swath hamper their application in timely CD to some extent, particularly for large areas. Therefore, it is of great interest to apply CD at both fine spatial and temporal resolutions (such as at Landsat spatial resolution and MODIS temporal resolution) with computer technologies, which is the objective of this paper. Note that, in this paper, we considered the Landsat spatial resolution (30 m) as “fine” relative to the MODIS spatial resolution (250 to 1000 m) and not in the absolute sense. This paper presents a framework of fast subpixel mapping (SPM) algorithms for CD, which borrows information from an available FRM. The rest of the introduction section follows the line of techniques related to subpixel resolution CD: existing spatiotemporal fusion, spectral unmixing-based CD, SPM-based CD, and the proposed fast SPM-based CD.

A. Spatiotemporal Fusion

Spatiotemporal fusion techniques [6]–[10] have been developed to blend fine spatial but coarse temporal resolution images with coarse spatial but fine temporal resolution images to generate an image with both fine spatial and temporal resolutions. Gao *et al.* [6] proposed STARFM to blend fine temporal resolution information from a MODIS image and fine spatial resolution information from a Landsat image. To enhance the performance of STARFM for heterogeneous landscapes, an enhanced STARFM was developed in [7]. For mapping forest disturbance, STARFM was extended with a spatial and temporal adaptive algorithm for mapping reflectance change that uses multiple Landsat images and a temporally dense stack of spatially coincident MODIS images [8]. In [9], sparse representation was applied to characterize the corresponding relationship between structures in the known fine spatial resolution Landsat images and the corresponding coarse spatial resolution MODIS images, and the unknown fine spatial resolution image was reconstructed through sparse coding. Song and Huang [10] superresolved a coarse spatial resolution MODIS image with sparse representation first, which was then fused with a known Landsat image by high-pass modulation to obtain a Landsat image on the prediction date.

The outputs of spatiotemporal fusion are remote sensing images in units of reflectance, which can act as an intermediate step toward CD: the resulting fused images can be further processed by existing CD techniques in [1]–[5] to monitor changes at a fine spatial and temporal resolution. Nevertheless, these spatiotemporal fusion models are usually built under different assumptions or for particular applications (e.g., mapping forest disturbance in [8]). They are performed with the hypothesis that there is fixed correspondence between the known fine spatial resolution image and the corresponding coarse spatial resolution image in the same area, and such correspondence is used to predict the unknown fine resolution image on other days. However, because of differences in the weather, atmosphere, and some other factors (e.g., uncertain natural changes and human activities) during data acquisition, it is sometimes difficult to obtain a reliable relationship between the fine and coarse resolution images, and in other cases, the relationship may not be constant over a long period (i.e., is temporally nonstationary).

B. Spectral Unmixing-Based CD

For the coarse spatial resolution image, each pixel covers a large area and generally contains more than one type of land cover class, that is, constitutes a mixed pixel. Mixed pixels are a common problem caused by limited spatial resolution. Mixed pixel analysis techniques, such as spectral unmixing [11], have been studied for decades to extract land cover information within mixed pixels. Spectral unmixing is a technique to estimate the proportions of land cover classes within each mixed pixel, and it has already been applied to CD [12]–[14]. With spectral unmixing, the proportions of each class in the coarse spatial but fine temporal resolution images can be estimated. The unmixing outputs derived from time-series images can inform users of by how much the proportion of each land cover class increases or decreases during a given period [15]. Employing spectral unmixing straightforwardly for CD,

however, one can only obtain quantitative information about the changes at the pixel level (i.e., coarse spatial resolution) and cannot determine detailed change information at a finer spatial resolution, that is, changes in the subpixel classes.

Note that, with the availability of fine spatial resolution land-use database LGN5, Zurita-Milla *et al.* [16] introduced an unmixing-based data fusion approach to produce images with the temporal resolution of MERIS and the spatial resolution of Landsat. Different from the standard spectral unmixing, however, the objective of such unmixing is to estimate endmembers (with the spectral resolution of MERIS) for each Landsat pixel, which can be assumed to be pure. This unmixing-based fusion produces fine spatial resolution images in units of reflectance, and it is essentially a type of spatiotemporal fusion technique.

C. SPM-Based CD

This paper focuses on subpixel resolution CD algorithms, which provide fine spatial resolution thematic maps of land cover changes. The framework of these algorithms is based on SPM. SPM (also termed superresolution mapping in remote sensing) is a technique to predict a hard-classified land cover map at a finer spatial resolution than that of the input coarse spatial resolution image [17], [18]. It can be achieved through the postprocessing of spectral unmixing: each coarse spatial resolution pixel is divided into multiple subpixels, and their class labels are predicted under the coherence constraint imposed by the outputs of spectral unmixing (i.e., coarse resolution land cover proportions).

SPM is often performed based on the spatial dependence assumption; the land cover is deemed to be spatially dependent both within and between pixels [17]. This hard classification (but at the subpixel resolution) technique has received increasing attention over the past decades, and many algorithms have been developed. Some SPM algorithms involve iterative optimization, including genetic algorithms [19], particle swarm optimization [20], PSA [21]–[26], Hopfield neural networks [27]–[30], and maximum *a posteriori* models [31]. They require several iterations and some time to approach a satisfactory result. Recently, a new type of SPM algorithm, named the soft-then-hard SPM (STHSPM) algorithm, has been introduced and summarized in [32]. The STHSPM algorithm consists of two steps: soft class value (between 0 and 1 for each class) estimation and hard class (0 or 1 for each class) allocation for each subpixel. Commonly used STHSPM algorithms include the SPSAM [33], [34], back-propagation neural networks [35]–[38], Kriging [39], indicator co-Kriging [40]–[42], and bilinear and bicubic interpolation-based methods [43], [44]. This type of SPM algorithm is noniterative (the iterations in the training process in a back-propagation neural network are not considered, as the training process is always offline). Therefore, SPM can be realized relatively quickly using STHSPM algorithms. In addition, SPM can be also achieved by a contouring [45]–[47] method and by a one-stage method that takes the raw image in units of reflectance as input and does not rely on spectral unmixing [48]–[51].

SPM is a promising technique for CD as it enables land cover changes between coarse spatial but fine temporal resolution images to be monitored at a finer spatial resolution and, thus, enables CD to be performed at both fine spatial and temporal resolutions. In recent years, several studies have been

conducted on this topic. Foody and Doan [52] studied forest cover changes in Brazil at 30 m Landsat spatial resolution, using two MERIS-like images (300 m). With the aid of a former FRM, Ling *et al.* [53] utilized a PSA to predict the land cover change at the subpixel resolution between bitemporal images. However, as aforementioned, both the Hopfield neural network and the PSA are optimization-based algorithms, which are iterative and time consuming. Using bitemporal Landsat and MODIS images, Li *et al.* [54] proposed a new Markov random field model for subpixel resolution CD of forests in the Brazilian Amazon basin. In this model, a temporal energy function characterized by transition probabilities during the studied period was added to the original Markov random field for SPM [48], [49]. This model is also iterative, and moreover, determination of the weights for the spatial and temporal energy functions is an open problem. Thus, there is a need for the development of real-time SPM algorithms for subpixel resolution CD in practical applications (e.g., CD at Landsat spatial resolution and MODIS temporal resolution). The objective of this paper was to develop fast SPM algorithms for subpixel resolution CD.

D. Proposed Fast STHSPM-Based CD With a Fine Resolution Map (FRM)

In this paper, for the first time, five fast STHSPM algorithms, including bilinear interpolation-, bicubic interpolation-, SPSAM-, Kriging-, and the recently developed RBF interpolation-based SPM [55] methods, are proposed for fine spatial and temporal resolution CD. In addition to the low computational burden, these five algorithms also have the advantage of not requiring prior class information on spatial structure.

Similar to spatiotemporal fusion, in this paper, the aforementioned five fast STHSPM algorithms for subpixel CD are developed based on the availability of fine spatial but coarse temporal resolution information. Unlike spatiotemporal fusion, however, the objective of the five STHSPM algorithms was to generate fine spatial resolution subpixel land cover maps, which were then compared with observed land cover changes at both fine spatial and temporal resolutions. We consider borrowing information from the thematic land cover map of the known fine spatial resolution image (i.e., FRM [53]), to decrease the uncertainty in SPM of coarse resolution images and further increase the accuracy of CD.

The main contributions of this paper are summarized as follows.

- 1) A framework of fast STHSPM algorithms is proposed for subpixel resolution CD. The fast STHSPM algorithm uses fine spatial resolution thematic information from an FRM for SPM of coarse images.
- 2) Different from [53] that only used FRM in the “former FRM and latter coarse image” case, the FRM is also considered in the “former coarse image and latter FRM” case and subpixel resolution CD between coarse images.

The remainder of this paper is organized as follows. Section II details the proposed five fast subpixel resolution CD methods, including how to incorporate an FRM in SPM to decrease the uncertainty in CD and the detailed methodology. Section III provides experimental results for three types of

image, and Section IV further discusses the proposed methods. Section V concludes this paper.

II. METHODS

A. Incorporating an FRM in SPM and Subpixel Resolution CD

As was done in [52], the subpixel resolution CD can be realized straightforwardly by SPM of multitemporal coarse spatial resolution images of the same area first and then comparing the generated subpixel maps with observed changes. However, the SPM problem is always underdetermined, with many multiple plausible solutions that can lead to an equally coherent recreation of the input coarse proportion image. Applying SPM to CD without any auxiliary information will result in many errors in the form of noise. In fact, for SPM of a single-date image, the accuracy can be enhanced by borrowing information from images before it and after it in time [18]. Such a scheme would be helpful to separate real changes from noise. Some studies demonstrated how to borrow information from coarse spatial resolution time-series images to enhance SPM [56]–[58]. Those studies, however, focused on enhancing SPM and were conducted with the assumption that there are no changes between the utilized coarse spatial resolution images.

Ling *et al.* [53] presented a method on using FRM to enhance subpixel resolution CD. In that study, however, only the historical FRM case was considered, and the subpixel resolution CD was implemented between different spatial resolution images (e.g., former Landsat and latter MODIS images). More importantly, different from the iterative PSA in [53], noniterative and fast subpixel resolution CD algorithms are proposed in this paper.

This paper extends the utilization of FRM to the following two cases.

- 1) The data acquisition date of the FRM is after that of the coarse spatial resolution image. Sometimes, users want to detect changes from a date earlier than that of the FRM, and only a coarse spatial resolution image is available on that date. It is, therefore, necessary to develop methods for SPM of former coarse spatial resolution images with the aid of a latter FRM.
- 2) Subpixel resolution CD is implemented between images with the same coarse spatial resolution, and the SPM results of both coarse images are obtained with the aid of the FRM. For CD during a certain period, on both the start and end days, there may be only coarse spatial resolution images. To detect changes at fine spatial resolution during that period necessitates the construction of SPM methods for those coarse resolution images.

The core idea of enhancing subpixel resolution CD with an FRM is to use the spatial distribution of subpixel classes in the FRM to modify the SPM results of coarse spatial resolution images on other dates. Specifically, the spectral unmixing-derived class proportion of each class within each coarse pixel is compared with the corresponding one (obtained by degradation) in the available FRM. According to the differences in the proportions, some locations at subpixel resolution are determined to be changed or unchanged for the class, and correspondingly, some subpixels are considered to belong or not belong to the class.

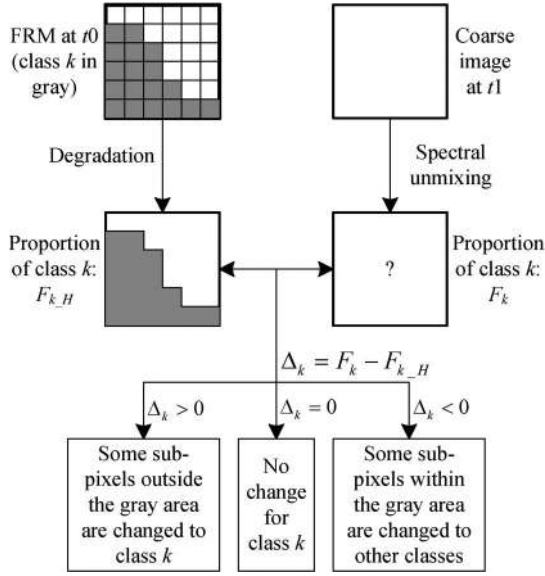


Fig. 1. Illustration of incorporating an FRM in SPM, where a single coarse pixel and class k is considered.

Suppose P_j ($j = 1, 2, \dots, M$, M is the number of pixels in the coarse image) is a coarse pixel and $F_k(P_j)$ is the coarse proportion of class k ($k = 1, 2, \dots, K$, K is the number of land cover classes in the studied area) for pixel P_j . Let S ($S > 1$) be the spatial resolution ratio between the coarse image and the FRM. The steps of incorporating the FRM in SPM are given in the following. Meanwhile, an example is provided in Fig. 1 to facilitate the illustration. In Fig. 1, a single coarse pixel and land cover information for class k is considered.

- 1) The FRM is degraded via an S by S mean filter (i.e., every S by S fine pixels are degraded to a coarse pixel) to synthesize the K coarse proportion images and the proportion for class k at pixel P_j , denoted by $F_{k-H}(P_j)$.
- 2) The differences in proportions $\Delta_k(P_j)$ are calculated

$$\Delta_k(P_j) = F_k(P_j) - F_{k-H}(P_j). \quad (1)$$

- 3) The changed and unchanged subpixel locations for each class are determined. The following three cases are taken into consideration.
 - a) If $\Delta_k(P_j) = 0$, there is no change for class k , and the spatial distribution of class k within P_j in the coarse image is the same as that in FRM (e.g., the gray area in Fig. 1).
 - b) If $\Delta_k(P_j) > 0$, the locations of fine pixels for class k in the FRM (e.g., the gray area in Fig. 1) are still assigned to class k in the coarse image, and some subpixels at the remaining locations are changed to class k .
 - c) If $\Delta_k(P_j) < 0$, all subpixels for class k in the coarse image are within the area for class k in the FRM, and some subpixels within that area are changed to other classes.
- 4) The aforementioned steps are implemented for all M coarse pixels and all K classes in the coarse image to generate the SPM result.

As shown in Fig. 1 and the steps aforementioned, the available FRM can be applied to SPM of the coarse image that is acquired either before or after the FRM. Moreover, the FRM

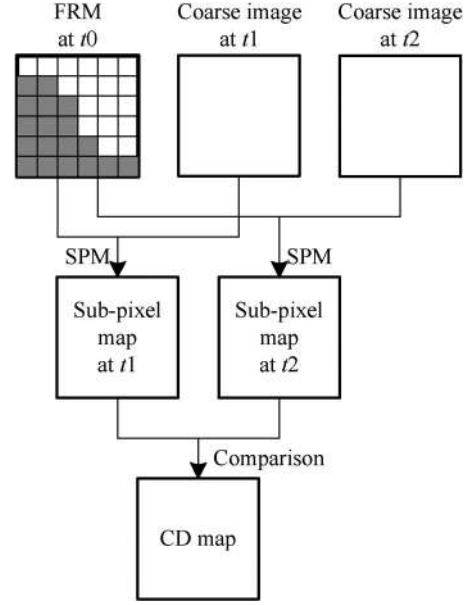


Fig. 2. CD between multitemporal coarse images with FRM.

can be used for SPM of multitemporal coarse images (see Fig. 2). Finally, the generated SPM results can be compared for the purpose of fine spatial and temporal resolution CD.

The critical step in utilizing an FRM in SPM is to determine which subpixels at the remaining locations are changed to class k ($k = 1, 2, \dots, K$) when $\Delta_k(P_j) > 0$ and which subpixels that are within the area for class k in the FRM are changed to other classes when $\Delta_k(P_j) < 0$. In this paper, those subpixels are found using the five fast STHSPM algorithms.

B. Fast STHSPM Algorithms

The STHSPM algorithm is a type of SPM algorithm that first estimates the soft class values and then allocates a hard class to each subpixel. This paper focuses on five noniterative and fast STHSPM algorithms: bilinear interpolation, bicubic interpolation, SPSAM, Kriging, and the recently developed RBF interpolation methods [55].

Similar to that in Section II-A, S denotes the zoom factor for SPM (i.e., each coarse pixel is divided into S by S subpixels). Suppose $p_{j,i}$ is the subpixel within coarse pixel P_j and $F_k(p_{j,i})$ ($0 \leq F_k(p_{j,i}) \leq 1$) is the soft class value for class k at subpixel $p_{j,i}$. With the coarse proportion images as input, the task of soft class value estimation is to estimate $\{F_k(p_{j,i}) | i = 1, 2, \dots, S^2; j = 1, 2, \dots, M; k = 1, 2, \dots, K\}$ at the target fine spatial resolution. The soft class values are estimated based on the assumption of spatial dependence as described above for the STHSPM algorithms. The bilinear and bicubic interpolation methods are widely available in packages like MATLAB, R, IDL, and some publicly available programming libraries. Here, the principles of SPSAM, Kriging, and RBF interpolation for soft class value estimation are introduced briefly.

SPSAM assumes that, for the same class, spatial attraction exists between subpixels and their neighboring coarse pixels. The soft attribute value is calculated in terms of attraction

$$F_k(p_{j,i}) = \frac{1}{N} \sum_{n=1}^N \frac{F_k(P_n)}{d(P_n, p_{j,i})} \quad (2)$$

where N is the number of neighboring coarse pixels, $d(P_n, p_{j,i})$ is the Euclidean distance between the centroids of pixel P_n and subpixel $p_{j,i}$, and $F_k(P_n)$ is the coarse proportion of class k at neighboring pixel P_n .

In Kriging-based SPM, the soft attribute value is a weighted linear combination of N observed values, i.e.,

$$F_k(p_{j,i}) = \sum_{n=1}^N \beta_n F_k(P_n) \quad (3)$$

where β_n is a weight that is estimated by solving the Kriging system [59].

The soft class value predicted by RBF interpolation is

$$F_k(p_{j,i}) = \sum_{n=1}^N \lambda_k(P_n) \phi(P_n, p_{j,i}) \quad (4)$$

in which $\phi(P_n, p_{j,i})$ is a basis function that reflects the spatial relation between subpixel $p_{j,i}$ and pixel P_n , and $\lambda_k(P_n)$ is the coefficient of class k for coarse pixel P_n . The basis function takes the Gaussian form

$$\phi(P_n, p_{j,i}) = e^{-d^2(P_n, p_{j,i})/a^2} \quad (5)$$

where a is a parameter. The coefficients $\lambda_k(P_1), \lambda_k(P_2), \dots, \lambda_k(P_N)$ are calculated by

$$\begin{bmatrix} \phi(P_1, P_1) & \phi(P_2, P_1) & \dots & \phi(P_N, P_1) \\ \phi(P_1, P_2) & \phi(P_2, P_2) & \dots & \phi(P_N, P_2) \\ \dots & \dots & \dots & \dots \\ \phi(P_1, P_N) & \phi(P_2, P_N) & \dots & \phi(P_N, P_N) \end{bmatrix} \times \begin{bmatrix} \lambda_k(P_1) \\ \lambda_k(P_2) \\ \vdots \\ \lambda_k(P_N) \end{bmatrix} = \begin{bmatrix} F_k(P_1) \\ F_k(P_2) \\ \vdots \\ F_k(P_N) \end{bmatrix} \quad (6)$$

where the elements in the first matrix are calculated in the same way as for (5). The preliminary soft attribute values obtained in (2)–(4) are normalized to fall within $[0, 1]$.

Let $B_k(p_{j,i})$ be the binary class value

$$B_k(p_{j,i}) = \begin{cases} 1, & \text{if subpixel } p_{j,i} \text{ belongs to class } k \\ 0, & \text{otherwise.} \end{cases} \quad (7)$$

For a particular coarse pixel, for example, P_j , the number of subpixels for class k , i.e., $E_k(P_j)$, is calculated by

$$E_k(P_j) = \text{round}(F_k(P_j)S^2) \quad (8)$$

where $\text{round}(\bullet)$ is a function that takes the integer nearest to \bullet . The sum of the numbers of subpixels for all K classes is S^2 . The hard class allocation step of the STHSPM algorithm aims to predict $\{B_k(p_{j,i}) | i = 1, 2, \dots, S^2; j = 1, 2, \dots, M; k = 1, 2, \dots, K\}$, according to the soft class values and class proportions constraint in (8).

This paper employs a recently developed approach that allocates classes for subpixels in units of classes (UOC) [32]. UOC is processed on the fine spatial resolution soft class value map of each class in turn and has the unique advantage of taking the intraclass spatial dependence into consideration while allocating classes. This class allocation method is fast and reproduces exactly the coarse proportion data. Specifically, a visiting order of all classes is specified by comparing the Moran's I of all K classes, and the classes with larger indices are visited first, as proposed in [32]. For each class, the index can be estimated

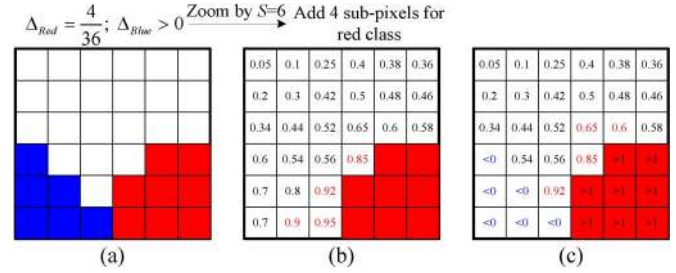


Fig. 3. Example to illustrate the adjustment (adjustment I) of soft class values to avoid class allocation conflict between classes. (a) FRM for the blue and red classes. (b) Class allocation result for the red class without adjustment I. (c) Class allocation result for the red class with adjustment I.

directly by using the proportion image of the given class. According to the visiting order of classes, the subpixels for the visited class are selected by comparing the soft class values for this class, and the subpixel with the largest soft class value is selected before those with smaller soft class values. The process for this class is repeated until all subpixels for it [the number is calculated by (8)] are completely exhausted. The remaining subpixels are then used for the allocation of the next class.

C. STHSPM-Algorithm-Based CD With an FRM

For the UOC-based class allocation method in the STHSPM algorithm, a subpixel map of each class is generated in turn, and these maps are integrated to produce the SPM result. Suppose that the soft class values have been already estimated by the STHSPM algorithms. Using an FRM as auxiliary information in STHSPM, for class k ($k = 1, 2, \dots, K$), the subpixel map is predicted by comparison of the soft class values at the remaining locations (e.g., outside the gray area in Fig. 1) when $\Delta_k(P_j) > 0$ and the soft class values within the area for class k in the FRM (e.g., the gray area in Fig. 1) when $\Delta_k(P_j) < 0$. Subpixels with larger soft class values for class k are more likely to be allocated to class k . During the process, two constraints inherently imposed by the SPM problem need to be satisfied.

- 1) Each subpixel should be assigned to only one class.
- 2) The number of subpixels for each class should be consistent with the coarse proportion data [see (8)].

To meet the aforementioned constraints, two adjustments, both of which are essential for UOC-based class allocation when using an FRM, are presented.

Adjustment I: Within a coarse pixel, in addition to $\Delta_k(P_j) > 0$, sometimes there are other classes (e.g., class k') with $\Delta_{k'}(P_j) \geq 0$. Similarly, the corresponding locations in the FRM for class k' should still be assigned to this class in the coarse image. For the $\Delta_k(P_j) > 0$ case, at the remaining locations, the subpixels with the largest soft class values for class k may be those that should be assigned to class k' . Fig. 3 gives an example to illustrate this issue. Let us consider two classes (i.e., red and blue) within a single coarse pixel, and $\Delta_{Red} = 4/36$, and $\Delta_{Blue} > 0$. The red class is assumed to be visited before the blue class. Fig. 3(a) is the FRM for the two classes. By zooming with $S = 6$, four subpixels should be allocated to the red class outside the red area when using the FRM. According to the soft class values in Fig. 3(b), the four subpixels with the largest values (marked in red) are assigned to the red class. As $\Delta_{Blue} > 0$, however, all six blue subpixels

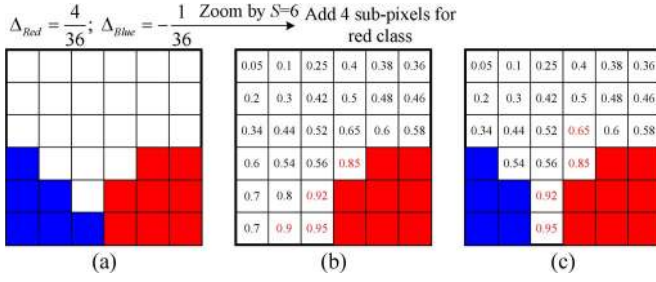


Fig. 4. Example to illustrate the adjustment (adjustment II) of visiting order of classes. (a) FRM for the blue and red classes. (b) Class allocation result for the red class without adjustment II. (c) Class allocation result for the red class with adjustment II.

should not change and should still be retained for the blue class during class allocation for the red class. In this case, the two subpixels with values 0.9 and 0.95 should not be assigned to the red class. To avoid such conflict, adjustment I is applied: the soft class values for the red class in the blue area need to be suppressed to be a very small value (any value less than 0) to ensure that the blue subpixels will not be allocated to the red class during class allocation. Meanwhile, the soft class values for the red class in the red area can be also modified to a very large value (any value greater than 1). After the adjustment, as shown in Fig. 3(c), no blue pixels are allocated to the red class, but another two subpixels with values 0.65 and 0.6 (marked in red) are allocated instead.

Adjustment II: Another example is provided in Fig. 4 to facilitate description. Again, the red and blue classes within a single coarse pixel are considered, and $\Delta_{Red} = 4/36$, and $\Delta_{Blue} = -1/36$. Assume that the calculated Moran index of the red class is larger than that of the blue class and that the red class should be visited before the blue class. With $S = 6$, four subpixels should be allocated to the red class outside the red area in Fig. 4(a). Fig. 4(b) marks the four soft class values of the four added subpixels for the red class. However, $\Delta_{Blue} = -1/36$ means that, of the six blue subpixels, five of them should still belong to the blue class. Therefore, at least one of the two subpixels with values 0.9 and 0.95 should not be assigned to the red class. To address this issue, adjustment II is applied: any class (e.g., class k') with $\Delta_{k'}(P_j) < 0$ needs to be visited before the class (e.g., class k) with $\Delta_k(P_j) \geq 0$. Fig. 4(c) shows the class allocation result for the red class, where the subpixel with a value of 0.95 is assumed not to belong to the blue class (according to the soft class values for the blue class), and the four added subpixels for the red class are marked in red.

The implementation steps of the proposed STHSPM-based algorithm for CD with an FRM are given here. Let us first take the former FRM (at t_0) and latter coarse image (at t_1) case as an example.

- Step 1) Spectral unmixing is conducted on the coarse image at t_1 , and the outputs are a set of coarse proportion images of classes (i.e., $\{F_k(P_j)|j=1, 2, \dots, M; k=1, 2, \dots, K\}$).
- Step 2) The coarse proportion images are downsampled with any of the five STHSPM algorithms, and the outputs are soft class values at the target fine spatial resolution (i.e., $\{F_k(p_{j,i})|i=1, 2, \dots, S^2; j=1, 2, \dots, M; k=1, 2, \dots, K\}$).

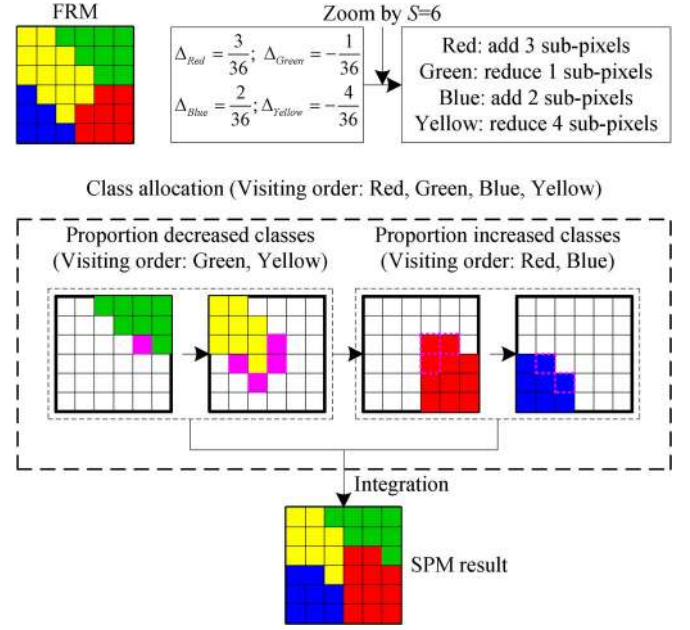


Fig. 5. Example of the whole flowchart of incorporating an FRM in STHSPM, where the deep pink subpixels are those not allocated to the green or yellow class.

- Step 3) Using the available FRM, UOC-based class allocation for the STHSPM algorithm is implemented to produce an SPM result at t_1 , where adjustment I and adjustment II are essential.
- Step 4) The predicted SPM result at t_1 is compared with the FRM at t_0 in terms of class labels for CD analysis.

For the former coarse image (at t_0) and latter FRM (at t_1) case, the steps are the same as listed above. With respect to the subpixel resolution CD between coarse images at, for example, t_1 and t_2 , the FRM at another time (e.g., t_0) is used for SPM of both coarse images independently, according to the aforementioned steps. The generated SPM results at t_1 and t_2 are finally compared for CD, as shown in Fig. 2. Fig. 5 exhibits an example of the whole flowchart of the proposed STHSPM algorithm with an FRM. The whole process does not involve any iteration.

III. EXPERIMENTS

Three datasets were used in three experiments for validation of the proposed five subpixel resolution CD methods. For the SPSAM and Kriging methods, the window sizes of the neighborhood were set to 3 and 5, as suggested by the repeated test and relevant literature [32], [41]. The parameters of the RBF method were set according to the parameter analysis in [55]: the parameter a in the basis function [see (5)] was set to 10, and the window size of the neighborhood was set to 5.

A. Experiment on Synthetic Coarse Proportion Images

1) *Dataset:* To control the analysis, a synthetic dataset was used in this experiment to test the proposed five STHSPM-algorithm-based CD methods with an FRM. Specifically, three Landsat images with 30 m spatial resolution acquired on three different days were classified to produce three 30 m land cover maps. One of the maps was used as the FRM. The coarse proportion images were created by degrading the other two 30 m

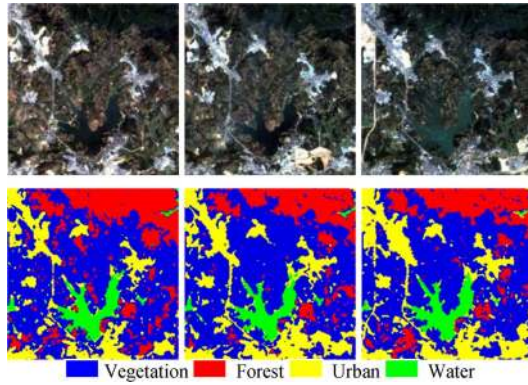


Fig. 6. Three Landsat images in Shenzhen, China, on three dates. (Left to right) t_0 on November 20, 2001, t_1 on November 7, 2002, and t_2 on November 23, 2005. (Line 1) Color image (bands 3, 2 and 1 as RGB). (Line 2) Hard-classified land cover maps.

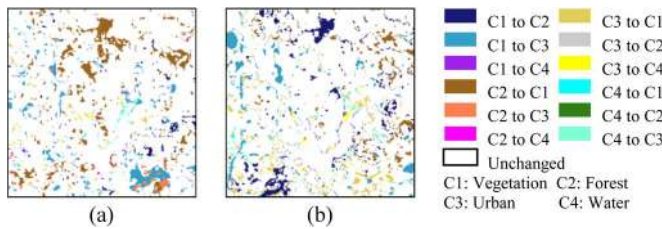


Fig. 7. Reference change maps. (a) From t_0 to t_1 . (b) From t_1 to t_2 .

classified maps via an S by S mean filter. SPM methods were implemented to recreate the 30 m land cover maps, by zooming in the proportion images with a zoom factor S . The generated SPM results were compared with the FRM, or they were mutually compared for CD analysis. The advantages of using synthetic coarse images are that the input proportions are error free and represent greater control in the test. Although this scheme does not represent a sufficiently real test of SPM and CD algorithms, the reference map is known perfectly and can be used to assess the accuracy of SPM prediction and CD. The test is directed at the SPM algorithm itself, which is appropriate at the method development stage [17].

The three 30 m Landsat images cover an area in Shenzhen, China. Registration and relative radiometric correction were conducted on the Landsat images. The selected study area is a heterogeneous region with 250×250 pixels and mainly covers four land cover classes: vegetation, forest, urban, and water. The three images were acquired on November 20, 2001 (t_0), November 7, 2002 (t_1), and November 23, 2005 (t_2), respectively. The images were classified with a supervised neural network to generate the 30 m reference land cover maps (provided by Dr. Y. Xu). The classification accuracy for all t_0 , t_1 , and t_2 reference maps was over 90%. Fig. 6 shows the three images and their corresponding classified land cover maps used as reference. The reference change maps from t_0 to t_1 and from t_1 to t_2 are shown in Fig. 7, in which “CA to CB” means that the pixel belongs to class A at the former time but changes to class B at the latter time.

2) *Benefits of Using an FRM in CD*: The changes from t_0 to t_1 were tested here. The 30 m reference land cover map at t_0 was used as an FRM, and the reference map at t_1 was degraded to synthesize coarse proportion images at t_1 . The 30 m map at t_1 was degraded with five mean filters, namely, 5×5 , 8×8 ,

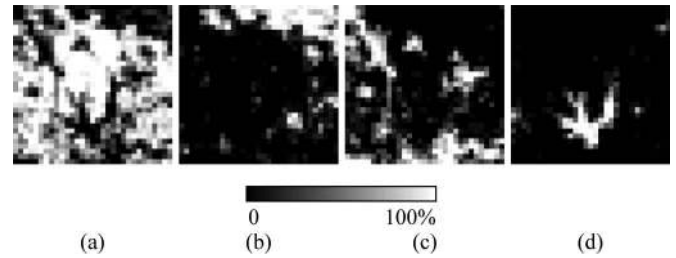


Fig. 8. Proportion images of the four classes at t_1 . (a) Vegetation. (b) Forest. (c) Urban. (d) Water.

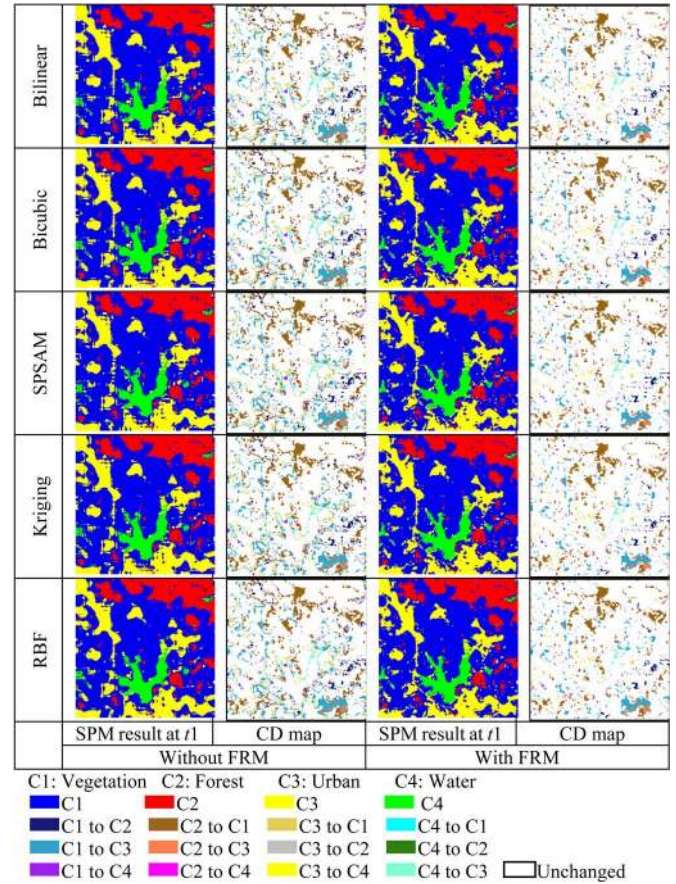


Fig. 9. SPM and CD results of the five STHSPM algorithms (from t_0 to t_1 , with the t_0 reference map as the FRM ($S = 8$)).

10×10 , 12×12 , and 15×15 pixels, to simulate proportion images with spatial resolutions of 150, 240, 300, 360, and 450 m. The five STHSPM algorithms were applied to restore the 30 m land cover map and then compared with the t_0 reference map for CD.

Fig. 8 shows the proportion images of four classes at 240 m spatial resolution, comparable with the spatial resolution of medium spatial resolution systems such as MODIS. As can be observed, the land cover information presented in these 240 m images is limited and insufficient for CD analysis. With these images as input and a zoom factor $S = 8$, the five STHSPM algorithms were implemented. The results are given in Fig. 9, where results of both the original version (i.e., without an FRM) and new version (i.e., with an FRM) algorithms are provided. The CD map for each method is also exhibited. For the five original STHSPM algorithms without FRM, there are many

TABLE I
SPM ACCURACY (%) OF t_1 IMAGE (t_0 REFERENCE MAP AS THE FRM) FOR THE FIVE STHSPM ALGORITHMS

	$S=5$		$S=8$		$S=10$		$S=12$		$S=15$	
	Without FRM	With FRM	Without FRM	With FRM	Without FRM	With FRM	Without FRM	With FRM	Without FRM	With FRM
Bilinear	81.99	86.33	80.07	86.49	79.74	86.36	78.39	86.18	76.63	85.90
Bicubic	82.67	86.50	80.61	86.55	80.02	86.42	78.67	86.26	77.15	86.00
SPSAM	81.90	86.24	79.37	86.18	78.95	86.10	77.93	85.95	76.02	85.81
Kriging	82.41	86.65	80.09	86.36	79.82	86.32	78.55	86.30	76.82	85.92
RBF	83.06	86.76	80.76	86.72	79.83	86.49	78.85	86.38	77.20	85.97

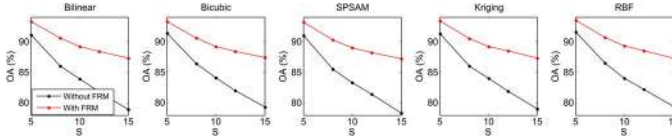


Fig. 10. CD accuracy of the five STHSPM algorithms (from t_0 to t_1 , with the t_0 reference map as the FRM).

linear artifacts and isolated pixels in the generated 30 m land cover maps, particularly for the forest and urban classes. Consequently, many pixels are incorrectly identified as changed pixels when compared with the 30 m map at t_0 time, as shown in the CD results in the second column in Fig. 9. Focusing on the maps of the new version STHSPM algorithms in the third column, however, we can see with the aid of the FRM that the generated SPM results are much closer to the reference map at t_1 in Fig. 6. The elongated features of urban class are well restored, and the boundaries of each class are smoother than those for the original STHSPM algorithms. Correspondingly, while referring to Fig. 7(a), the CD maps of STHSPM algorithms with an FRM in the fourth column are found to be very close to the reference CD map (see, for example, the distribution of the “vegetation to urban” and “water to vegetation” classes). Visual comparison confirms the benefit of using an FRM in STHSPM-algorithm-based CD.

Table I gives the SPM accuracy of the five STHSPM algorithms for all five zoom factors. The pure coarse resolution pixels in Fig. 8 were ignored in the accuracy statistics as pure pixels increase the accuracy without providing any useful information on the performance of the SPM methods [19], [32]. As concluded from the table, using an FRM, the SPM accuracy increases noticeably. For example, the SPM accuracy of the five STHSPM algorithms increases by around 4% for $S = 5$ and around 9% for $S = 15$.

The OA of CD was calculated from the full transition error matrix and is provided in Fig. 10. From this figure, three observations can be made. First, for all five zoom factors, greater CD accuracy is produced when the FRM is incorporated in the STHSPM algorithms. This is attributed to the fact that the FRM decreases the inherent uncertainty in SPM, as shown in Table I. Second, as S increases, no matter whether the FRM is used or not, the CD accuracy of the five STHSPM algorithms decreases. This is because the complexity of the SPM task increases when S becomes larger, which propagates to the post CD analysis. Third, the accuracy gain of using the FRM increases as S increases. More precisely, the accuracy gain increases stably from 2% for $S = 5$ to 8% for $S = 15$. Through the above experiments, it was shown that using an FRM can increase SPM

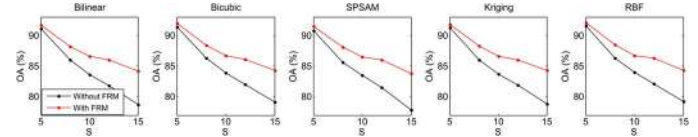


Fig. 11. CD accuracy of the five STHSPM algorithms (from t_0 to t_2 , with the t_0 reference map as the FRM).

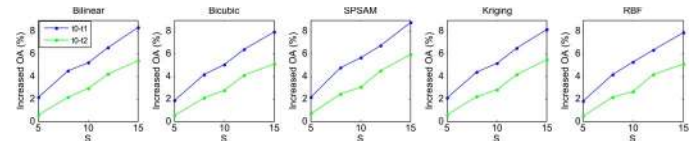


Fig. 12. CD accuracy gain by using FRM for t_0 to t_1 and t_0 to t_2 cases (with the t_0 reference map as the FRM).

accuracy and the subpixel CD accuracy for all five STHSPM algorithms.

3) *CD for a Long Period:* Here, the changes from t_0 to t_2 are tested for a longer period (i.e., four years) than from t_0 to t_1 . The 30 m t_0 reference map was used as the FRM, and the coarse proportion images at t_2 were synthesized by degrading the 30 m t_2 reference map. Again, five zoom factors were analyzed: $S = 5, 8, 10, 12$, and 15 . The CD accuracy of the five STHSPM algorithms without an FRM and with an FRM is shown in Fig. 11. Similarly, with an FRM, the STHSPM algorithms were able to produce greater CD accuracy for all zoom factors. The accuracy of all ten methods decreases as S increases, but the five methods without an FRM decreases more rapidly. The accuracy gain by using an FRM in this experiment was compared with that in the last experiment. As shown in Fig. 12, for each zoom factor, the accuracy gains for all five STHSPM algorithms from t_0 to t_2 are, as expected, smaller than for t_0 to t_1 . For example, for $S = 5$, with the aid of the FRM, for CD from t_0 to t_2 , the accuracy increases by less than 1%, whereas for CD from t_0 to t_1 , the accuracy increases by over 2%. For larger zoom factors, the differences between the two periods are even larger, and when $S = 15$, the differences are greater than 2%. As changes in land cover can be complicated, the uncertainty in CD increases for longer periods correspondingly. The results in this experiment reveal that the FRM imparts greater benefits for SPM of coarse images that are acquired on temporally proximate days.

4) *CD for the Former Coarse Image and Latter FRM Case:* In the previous two experiments, the acquisition date of the FRM precedes that of the coarse images. As mentioned in Section II-A, it is necessary to develop SPM methods for a preceding coarse spatial resolution image (i.e., no fine spatial

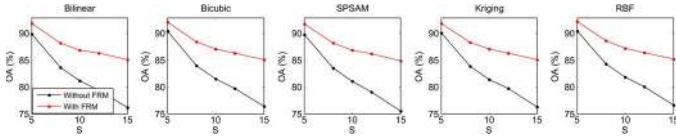


Fig. 13. CD accuracy of the five STHSPM algorithms (from t_0 to t_1 , with the t_1 reference map as the FRM).

resolution images are available at the former time) with the aid of a latter FRM. In this experiment, we test the case where the FRM was acquired after the coarse images. The changes from t_0 to t_1 were tested in this experiment, but the 30 m t_1 reference map was used as the FRM. The former coarse proportion images at t_0 time were synthesized by degrading the 30 m t_0 reference map. Five zoom factors, namely, 5, 8, 10, 12, and 15, were tested. The generated SPM results of the five STHSPM algorithms were then compared with the latter 30 m t_1 map for CD.

The CD accuracy for all cases (i.e., two versions of five STHSPM algorithms with five zoom factors) is given in Fig. 13. It can be observed that, for all STHSPM algorithms with the FRM at a latter time, greater accuracy can still be obtained for each zoom factor. This illustrates that the data acquisition date order of coarse images and the FRM is not restricted for enhancing subpixel resolution CD, and the proposed five STHSPM-algorithm-based CD methods with an FRM are also applicable to an earlier coarse resolution image and latter FRM case.

It is worth noting that the accuracy of all cases with FRM in Fig. 13 is lower than the corresponding cases in Fig. 10, where the CD accuracy from t_0 to t_1 is also presented. For $S = 5$, with FRM, the accuracy of each STHSPM algorithm in Fig. 13 is around 1.5% lower than that in Fig. 10, whereas for $S = 15$, the difference is around 2%. The reason for this phenomenon is that SPM of the t_0 coarse images is conducted in Fig. 13, whereas SPM of the t_1 coarse images is conducted in Fig. 10. As shown in the 30 m t_0 and t_1 reference maps in Fig. 6, in some areas (such as the center area), there are small blocky features for the forest class in the t_0 reference map, but they changed to vegetation pixels in the t_1 reference map. In the t_1 coarse image, coarse pixels in these areas are pure pixels, but mixed pixels in the t_0 coarse image. Using the t_1 map as the FRM for SPM of the t_0 coarse images, the SPM results for the mixed pixels are still the same as those without the FRM. Therefore, pure pixels in the degraded FRM cannot help to increase the accuracy of SPM of the corresponding mixed pixels in other coarse resolution images.

5) CD Between Coarse Images: From Section III-A2–A4, CD was carried out between fine and coarse spatial resolution images, for the case where a fine spatial resolution image is available on either the start or the end day during the studied period. Different from those three experiments, the subpixel resolution CD here was implemented between coarse resolution images, for the case where there is no fine spatial resolution image on the start or the end day during the studied period. Specifically, the 30 m t_1 and t_2 reference maps were degraded to synthesize the coarse proportion images at t_1 and t_2 . Five zoom factors (i.e., $S = 5, 8, 10, 12$, and 15) were considered. The t_0 reference map was used as the FRM for the SPM of both the t_1 and t_2 coarse resolution images. Finally, changes between t_1 and t_2 were detected.

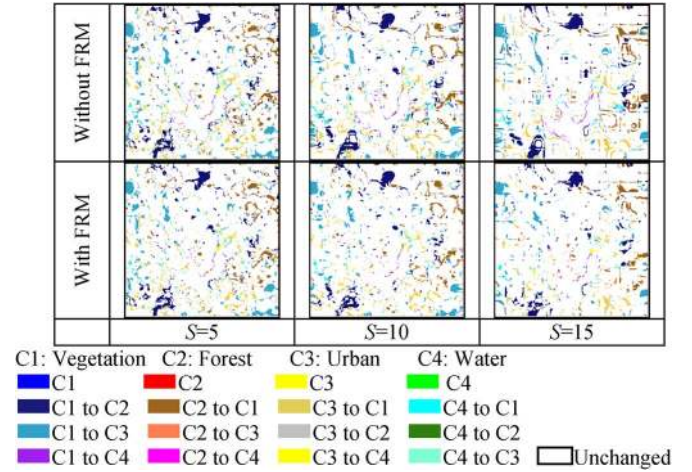


Fig. 14. CD results of the RBF interpolation-based SPM algorithm (from t_1 to t_2 , with the t_0 reference map as the FRM).

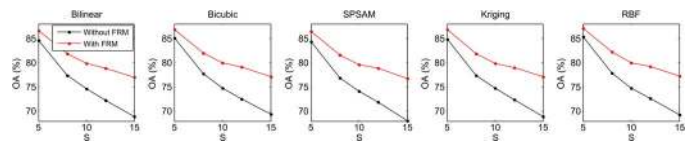


Fig. 15. CD accuracy of the five STHSPM algorithms (from t_1 to t_2 , with the t_0 reference map as the FRM).

Fig. 14 shows the 30 m CD results of one of the five STHSPM algorithms (i.e., RBF interpolation-based SPM). Comparing the CD results in Fig. 14 with the reference in Fig. 7(b), we can clearly observe that without the FRM, the results contain many errors propagated from the SPM results of the t_1 and t_2 coarse images. Particularly, for a large zoom factor (e.g., $S = 15$), many changed pixels in the CD result appear incorrectly as circular features. Using an FRM for both the t_1 and t_2 coarse images, the generated CD results seem more accurate while referring to Fig. 7(b), and the advantages become more obvious as S increases. A quantitative evaluation for all five STHSPM algorithms is provided in Fig. 15. Consistent with visual assessment, the FRM can help to increase the CD accuracy, and the increase is also obvious for the other four STHSPM algorithms. More precisely, the accuracy gain of using an FRM for the five STHSPM algorithms increases from about 2% for $S = 5$ to 8% for $S = 15$. This subsection, thus, demonstrates that it is helpful to use an FRM in CD between coarse images.

6) Comparison With Other Methods: The proposed five STHSPM algorithms with an FRM were compared with the PSA-based CD with an FRM [53]. To illustrate the accuracy gain of subpixel resolution CD, a conventional pixel-based CD method was compared with the proposed algorithms, in which SPM results were produced by a pixel-based classification (HC), and CD was performed by comparing the former and latter fine spatial resolution maps. In the HC method, all subpixels within a coarse pixel were assigned to the class with the largest proportion. The changes from t_0 to t_1 (with the t_0 reference map as the FRM) and from t_1 to t_2 (with the t_0 reference map as the FRM) were tested for comparison of the total of seven CD methods.

The CD accuracy of the seven methods is exhibited in Fig. 16. Obviously, the accuracy of the six SPM algorithms

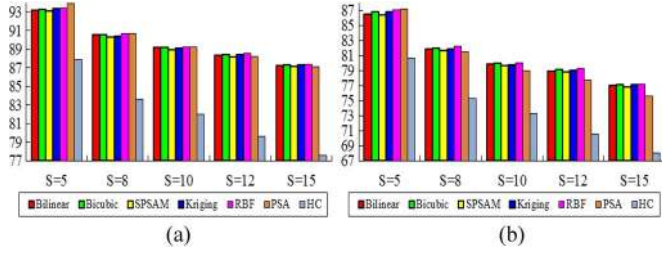


Fig. 16. CD OA (%) of the six SPM algorithms with an FRM (with the t_0 reference map as the FRM) and the conventional pixel-based HC approach. (a) From t_0 to t_1 . (b) From t_1 to t_2 .

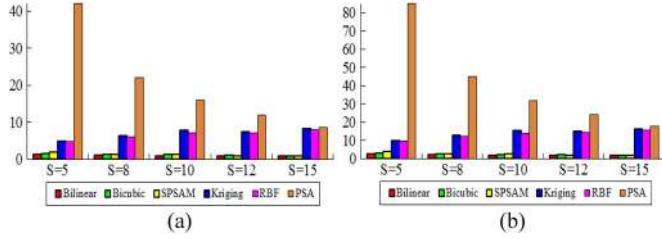


Fig. 17. Computing time (in seconds) of the six SPM algorithms with an FRM (with the t_0 reference map as the FRM). (a) From t_0 to t_1 . (b) From t_1 to t_2 .

is higher than that of the HC-based CD method. Generally, with an FRM, all five STHSPM algorithms were found to have very close accuracy for each zoom factor (see the two subfigures). From the bar charts in Fig. 16(a), it can be seen that PSA tends to achieve higher accuracy than the five STHSPM algorithms for $S = 5$, but for larger zoom factors, there are minor differences between the six methods. With respect to the CD accuracy for t_1 to t_2 in Fig. 16(b), PSA produces slightly lower accuracy than the five STHSPM algorithms.

Fig. 17 shows the computing time of the six SPM methods. All methods were tested on an Intel Core 2 processor (1.80-GHz Duo central processing unit, 2.00-GB random access memory) with MATLAB version 7.1. For CD from t_0 to t_1 , SPM was conducted only on the t_1 coarse images, whereas from t_1 to t_2 , SPM was conducted on both the t_1 and t_2 coarse images. Thus, the computing time in Fig. 17(b) doubles that in Fig. 17(a) in general. Note that the computing time of PSA decreases as S increases. This is because PSA swaps subpixels within the coarse pixel and it is implemented in units of coarse pixels. The computing efficiency of PSA is mainly related to the size of coarse image and not affected much by the number of subpixels within each coarse pixel. For $S = 5, 8, 10, 12$, and 15 in the experiments, the size of the coarse images (by degradation of the 250×250 pixel reference maps) are 50×50 , 31×31 , 25×25 , 20×20 , and 16×16 , respectively. The decreasing size leads to the decreasing computing time of PSA as a result. Examining the results in Fig. 17, we find that the five STHSPM algorithms are faster than PSA and that the bilinear, bicubic, and SPSAM methods are much faster. All five STHSPM algorithms require less than 10 s for CD from t_0 to t_1 and less than 20 s for CD from t_1 to t_2 . With respect to the bilinear, bicubic, and SPSAM methods, less than 5 s is required in all cases in Fig. 17. The high efficiency of the five STHSPM algorithms is attributed to their noniterative character. This validates that the five STHSPM algorithms with an FRM are fast for subpixel CD applications.

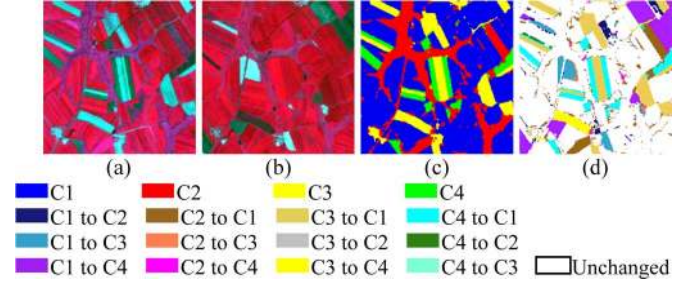


Fig. 18. Two Landsat images covering the same area in Liaoning, China. (a) False color image (bands 4, 3, and 2 as RGB) in August 2001 (t_0). (b) False color image (bands 4, 3, and 2 as RGB) in August 2002 (t_1). (c) Hard-classified land cover map at t_0 time, where blue, red, yellow, and green denote classes C1, C2, C3, and C4, respectively. (d) CD reference map from t_0 to t_1 .

B. Experiment on Degraded Multispectral Images

1) *Dataset*: The data used in this experiment are two 30 m multispectral Landsat images. This experiment is designed to consider the inevitable uncertainty in spectral unmixing, which can propagate to the post SPM and CD processes. One 30 m multispectral Landsat image was degraded band by band via an S by S mean filter to simulate a coarse multispectral image. Spectral unmixing was then conducted on the coarse images to generate proportion images, which were used as the input of SPM. With the zoom factor S , SPM was performed to predict the 30 m fine spatial resolution map. The hard-classified land cover map of the other 30 m multispectral Landsat image was used as the FRM. With respect to the reference change map, it was obtained by comparison of the two hard-classified maps of the corresponding 30 m multispectral images.

The two 30 m multispectral images were acquired by the Landsat-7 enhanced thematic mapper plus sensor in August 2001 (t_0) and August 2002 (t_1) in the Liaoning Province of China. The t_0 image was registered to the t_1 image, and then, the histogram matching method was implemented for the relative radiometric correction [60]. The studied area covers 200×200 pixels, and four land cover classes can be identified, which are denoted by C1, C2, C3, and C4. The two images are shown in Fig. 18(a) and (b), respectively. A supervised neural network was applied to the two Landsat images to generate the 30 m reference land cover maps. The classification accuracy for the two reference maps was over 90%. The t_0 and t_1 reference maps and the reference change map (produced by comparing t_0 and t_1 reference maps) are shown in Fig. 18(c) and (d), respectively.

2) *Results*: The t_1 30 m multispectral Landsat image was degraded with an 8×8 pixel mean filter to produce a 240 m MODIS-like image. Fully constrained least squares linear spectral mixture analysis [61] has a simple physical meaning and is convenient in application. Thus, it was employed for spectral unmixing in the experiments. The generated proportion images of the four classes are exhibited in Fig. 19. The five STHSPM algorithms were implemented to recreate the 30 m land cover map at t_1 . In the experiments, the t_0 reference map in Fig. 18(c) was used as the FRM.

Fig. 20 gives the SPM and CD results of the RBF method. To illustrate the influence of spectral unmixing, the results for the degraded land cover map (the experimental procedure is the same as in Section III-A) are also presented in Fig. 20 for visual comparison. Checking the results in this figure, we see that, due

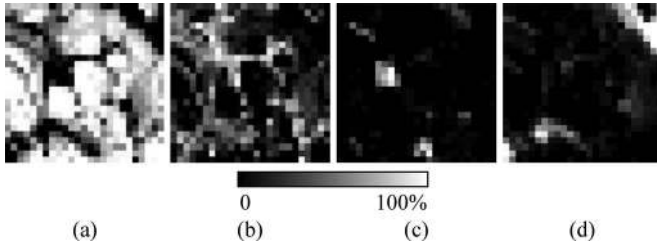


Fig. 19. Proportion images of the four classes at t_1 . (a) C1. (b) C2. (c) C3. (d) C4.

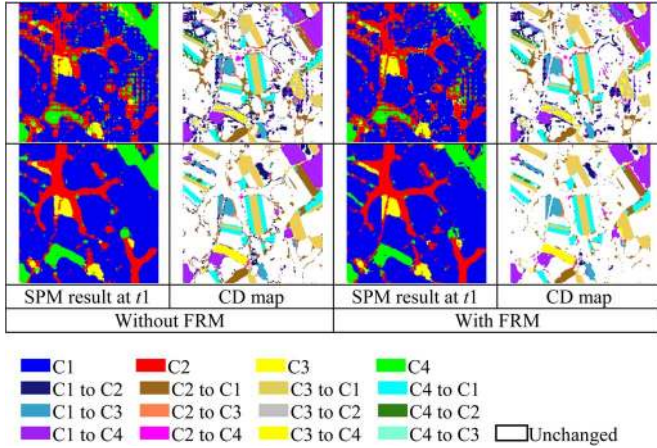


Fig. 20. SPM and CD results of the RBF interpolation-based SPM algorithm. (Line 1) Degraded Landsat image. (Line 2) Degraded land cover map.

TABLE II
CD ACCURACY (%) (WITH THE t_0 REFERENCE
MAP AS THE FRM) IN EXPERIMENT 2

	Degraded Landsat image		Degraded land cover map	
	Without FRM	With FRM	Without FRM	With FRM
Bilinear	77.06	78.13	91.47	93.01
Bicubic	77.26	78.21	91.73	93.13
SPSAM	77.18	78.13	91.56	93.16
Kriging	77.17	78.14	91.75	93.10
RBF	77.18	78.18	92.21	93.26

to the errors imposed by spectral unmixing, some scattering of pixels exists in the SPM results and the corresponding CD maps contain some noise. Using the FRM, for both cases, the produced SPM results seem more continuous, and more linear features are restored, particularly for class C2 (in red), and the CD results are closer to those in Fig. 18(d). Table II lists the OA of CD (calculated from the full transition error matrix) of all five STHSPM algorithms for both the degraded multispectral image and degraded land cover map cases. As shown in the table, because of the errors from spectral unmixing, when compared with the degraded land cover map case, the CD accuracy for the degraded multispectral image case decreases by around 15%. Nevertheless, for both cases, using the FRM, the proposed five STHSPM algorithms are able to produce greater CD accuracy. Particularly, for the degraded multispectral image case, the CD accuracy of five STHSPM algorithms increased from 77.1% to 78.1%. The experiment here suggests that FRM is also helpful for the subpixel resolution CD case where inherent uncertainty in spectral unmixing exists.

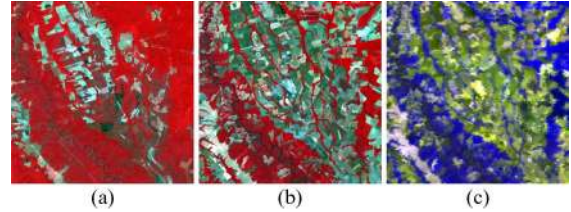


Fig. 21. Landsat-MODIS images (bands 4, 3, and 2 as RGB). (a) Landsat image acquired in July 1988. (b) Landsat image acquired in July 2005. (c) MODIS image acquired in July 2005.

TABLE III
CD ACCURACY (%) FOR THE REAL LANDSAT-MODIS IMAGES

	Bilinear	Bicubic	SPSAM	Kriging	RBF
Without FRM	72.28	72.22	72.34	72.27	72.22
With FRM	73.55	73.51	73.58	73.54	73.51

C. Experiment on Real Landsat-MODIS Images

In this experiment, a set of Landsat-MODIS images, including two Landsat images and one MODIS image, was used to test the proposed subpixel resolution CD algorithms for a real case. The study area is a $67.5 \text{ km} \times 67.5 \text{ km}$ tropical forest area in Brazil. One Landsat image acquired in July 1988 (t_0) was used as the source of the FRM, and the other Landsat image acquired in July 2005 (t_1) was used as the reference. The five STHSPM algorithms were implemented on the one single eight-day surface reflectance MODIS image acquired in July 2005 to predict the SPM result with the Landsat spatial resolution (i.e., 30 m) at t_1 time. The SPM result at t_1 time was compared with the former FRM for CD from t_0 to t_1 .

The original MODIS image has a spatial resolution of 463 m and was reprojected into the Universal Transverse Mercator coordinate system and then resampled to a spatial resolution of 450 m using the nearest neighbor algorithm [13]. Registration was conducted on the two Landsat images, and the errors were less than 0.5 pixel. The zoom factor of SPM for the MODIS image was set to 15 to predict a land cover map at 30 m spatial resolution. The spatial size of the MODIS image is 150×150 pixels, and the Landsat image is 2250×2250 pixels. Fig. 21 shows the three images.

The MODIS image was unmixed with fully constrained least squares linear spectral mixture analysis [61]. For the studied tropical forest area, proportion images of two main classes, i.e., forest and nonforest, were used as input to the SPM. For each 30 m Landsat image, the pixels were supposed to be pure materials, and an unsupervised k -means classifier was employed to generate the 30 m fine spatial resolution thematic map. The 30 m t_0 map was used as the FRM in this experiment, and the reference change map was produced by comparing the 30 m t_0 and t_1 reference maps.

Table III gives the CD accuracy for the five STHSPM algorithms. As shown in the table, without FRM, the CD accuracy of each STHSPM algorithm is around 72.2%. Incorporating FRM in SPM, all five algorithms produce greater accuracy, and the accuracy gains are around 1.3%. To study the effect of errors from spectral unmixing and the reference, the 30 m t_1 reference map was degraded with a factor of 15 to simulate the spectral unmixing result at 450 m spatial resolution. The CD accuracy of the five STHSPM algorithms resulting from

such a design is over 95%, regardless of the use of FRM. For the test of real Landsat–MODIS images in this experiment, due to the uncertainty in spectral unmixing (originating from the point spread function of the MODIS sensor and the unmixing algorithm itself, etc.) and the reference maps (both the FRM and the t_1 reference map), the CD accuracy of the proposed algorithms decreases by 23%.

IV. DISCUSSION

A. Differences Between the Proposed Methods and Spatiotemporal Fusion Techniques

As mentioned in the introduction, a major difference between the proposed methods and spatiotemporal fusion is that the five STHSPM algorithms yield subpixel maps, whereas spatiotemporal fusion yields images in units of reflectance. The objective of spatiotemporal fusion is to produce new multispectral images, which can be used for various goals, including monitoring changes in environmental variables and vegetation phenology. Some spatiotemporal fusion approaches were developed based on the strict assumption that there are no land cover changes during the studied period [16]. Specifically, all coarse images (e.g., MERIS images) in the studied period are assumed to have the same land cover distribution, which can be obtained from an FRM (e.g., LGN5). The FRM is degraded to provide the coarse proportions, and the ultimate task is to estimate the reflectance for each fine pixel, given the input MERIS reflectance. The reflectance of the fine spatial resolution time-series images can be compared to monitor the vegetation dynamics, surface temperature and surface soil moisture, and other environmental variables. Some other spatiotemporal fusion approaches relax the strong assumption that there are zero land cover changes during the studied period. Alternatively, they extract correspondence between the known fine and coarse spatial resolution images, to guide the prediction of fine spatial resolution images on other dates. It would be very promising to apply standard land cover CD techniques to the outputs of this type of spatiotemporal fusion, although very few studies (to the best of our knowledge) have been directed at this problem. For simplicity, we denote the latter spatiotemporal fusion as image pair-based spatiotemporal fusion. Consequently, the proposed methods are constructed to detect land cover changes, whereas spatiotemporal fusion techniques (e.g., image pair-based spatiotemporal fusion) are capable of detecting changes of both land cover and reflectance of fine pixels.

The image pair-based spatiotemporal fusion has potential in subpixel resolution CD. This necessitates a discussion about the differences between it and the proposed methods. An important difference is the restriction on the acquisition date of the known fine spatial resolution image. For image pair-based spatiotemporal fusion, at least one pair of fine–coarse spatial resolution (e.g., Landsat–MODIS) images of the same area is required. They have to be acquired on very close dates to ensure that there are almost zero changes between the scene covered by the two different spatial resolution images. This is because image pair-based spatiotemporal fusion techniques need to exploit the correspondence between the known fine and coarse spatial resolution images. For example, in the experiment in Section III-C, if implementing image pair-based spatiotemporal fusion, the MODIS image acquired on a date closer to that in Fig. 21(a) is

required. However, due to cloud contamination, time inconsistency of image acquisitions, and some other reasons [10], high-quality image pairs cannot always be guaranteed. By contrast, it is not the case for the five STHSPM algorithms using an FRM, as they do not necessarily need a pair of fine–coarse spatial resolution images.

B. Uncertainties in FRM

An FRM is required in the proposed method to aid the SPM process applied to coarse resolution images and increase CD accuracy. It is necessary to consider the reliability of the FRM. In this paper, the FRMs were obtained by hard classification of the fine spatial resolution multispectral image. Specifically, the supervised neural network was employed in the first two experiments, and the unsupervised k -means classifier was employed in the third experiment to classify the Landsat images. The stochastic processes, such as random initialization of the connection weightings between neurons in the neural network and cluster centers in the k -means classifier, may bring uncertainties in the produced FRM.

It is known that mixed pixels exist inevitably in remote sensing images [62], and such a means of producing the FRM involves inherent uncertainties. Nevertheless, it should be noted that the source of FRM (i.e., fine spatial resolution multispectral image) is generally selected according to the desired spatial resolution (defined by investigators) for SPM and CD. For example, given a 250 m spatial resolution MODIS image at t_1 , if the desired spatial resolution of SPM and subpixel CD is 30 m (zoom factor $S = 8$), we can seek a 30 m Landsat image for the source of FRM at t_0 ; if the desired spatial resolution is 10 m ($S = 25$), a 10 m SPOT image can be considered as the source of FRM at t_0 .

When defining 30 m as the desired target spatial resolution for SPM of a 250 m MODIS image at t_1 , if there are no 30 m Landsat images at t_0 , a finer spatial resolution image (if available), such as a WorldView or a QuickBird image, would be an effective alternative for the source of FRM at t_0 . In this case, the approximate 1 m FRM needs to be upsampled to 30 m to meet the required spatial resolution of SPM at t_1 . Since a 1 m FRM is available, an arising question is whether it is feasible to conduct SPM and subpixel resolution CD directly at a 1 m spatial resolution to obtain more detailed land cover information. For this issue, two factors are worthy of consideration: the zoom factor for SPM and the reliability of the FRM. First, it is suggested that the zoom factor S for SPM should not be too large, as within each coarse pixel the number of variables for SPM is S^2 and the uncertainty in SPM increases with increasing S . Second, classification accuracy often decreases with increasing spatial resolution, because smaller pixels may resolve within-class variation that leads to confusion between classes [63]. For example, for soil patches within a field of cereals, investigators may wish the whole field to be classified as cereals [63]. Therefore, by hard classification of very fine spatial resolution (e.g., 1 m) images, the derived FRM at t_0 may contain some scattering of pixels within large objects and result in an SPM result at t_1 with significant noise.

C. Limitations to the Method of Using an FRM

There are several limitations to the method of using an FRM. First, as indicated in Section III-A4, for SPM of the mixed

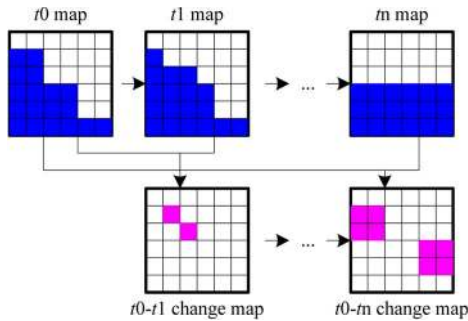


Fig. 22. Example for illustration of the land cover changes (deep pink pixels) during a long period (t_0 to t_n), where the land cover proportion of the blue class is fixed from t_0 to t_n .

pixels in coarse resolution images, the corresponding pure pixels in the degraded FRM cannot provide useful additional information. This case can occur where, for example, from the time of FRM to the time of the coarse image for SPM, there are new classes in those coarse pixels or even the whole studied area. For example, we suppose that there are four classes (i.e., vegetation, forest, urban, and water) in the FRM at t_0 and five classes (i.e., soil, vegetation, forest, urban, and water) in the coarse image for SPM at t_1 . That is, the new class soil is produced from t_0 to t_1 . As shown in Fig. 1, no information can be borrowed from the FRM for SPM of the new class soil, because all coarse soil proportions in the FRM are zero (i.e., no “gray area” for the soil class in the FRM). Therefore, the proposed method of using an FRM cannot enhance SPM of the new classes during the studied period of CD, but can enhance SPM of the other classes.

Second, the results in Section III-A3 show that the FRM tends to be more helpful for CD during a short period. This is explained by an example in Fig. 22. Suppose that, in a coarse pixel, the proportion of the blue class during a long period from t_0 to t_n does not change (i.e., $\Delta = 0$), but in the real-world case, the distribution of fine spatial resolution blue pixels gradually evolves. Eventually, at t_n time, the distribution of those fine pixels is quite different from that at the beginning t_0 time. This conflicts with the assumption that, if for the blue class $\Delta = 0$, there is no change for blue fine pixels and the spatial distribution of the blue class in the FRM can be copied directly to the coarse pixel at other times. Nevertheless, as observed from the changes (deep pink pixels) in Fig. 22, for a time close to t_0 (such as t_1), the changes are very small when compared with t_0 . Therefore, we can conclude that the rules in Fig. 1 and Section II-A of using FRM may be more appropriate for coarse images acquired on dates that are sufficiently close to that for the FRM. The sufficiently close dates can also ensure fewer new classes, as discussed above.

D. Future Research

Future research will be directed at two aspects: developing new STHSPM-based algorithms for CD with an FRM and seeking new approaches to acquire a reliable FRM.

Through the experiments, the proposed five STHSPM algorithms (i.e., bilinear, bicubic, SPSAM, Kriging, and RBF methods) were shown to be effective in using an FRM for subpixel resolution CD. As shown in Section II-C, any STHSPM algorithm has potential for subpixel resolution CD by incorporating

an FRM. Apart from the mentioned five STHSPM algorithms introduced in this paper, there exist some other STHSPM algorithms, such as the learning-based back-propagation neural network and indicator co-Kriging. They generally need prior spatial structure information (or some other alternatives [64]) on the land cover classes. With the availability of such information, they can be also applied for subpixel resolution CD.

The FRM information cannot only be derived directly from a multispectral image but also from some other data. Aplin and Atkinson [65] used land-line digital vector data to develop two per-field classification-based SPM approaches. Recently, Mahmood *et al.* [66] have developed another per-field classification-based SPM method, where a segmentation map generated from a fine spatial resolution color image was employed in the same way as the land-line digital vector data in [65]. Robin *et al.* [67] also utilized ancillary fine spatial resolution structural information in the form of a segmentation map for SPM, based on Bayes’ rule and the maximum *a posteriori* criterion. All these types of fine spatial resolution boundary information associated with the coarse image are probably able to produce a reliable FRM for CD. How to acquire such information and convert it to a reliable FRM seems to be a promising avenue for future research.

V. CONCLUSION

In this paper, based on the availability of a land cover map obtained from an available fine spatial resolution image (i.e., the FRM), five noniterative and fast STHSPM algorithms (i.e., bilinear-, bicubic-, SPSAM-, Kriging-, and RBF-based SPM methods) were proposed for subpixel resolution land cover CD. The FRM was taken into account not only in the case of a former FRM and latter coarse image but also in the case of a former coarse image and latter FRM, as well as the case of CD between coarse images. The STHSPM algorithms determined the subpixels for each class by comparing the soft class values and referring to the hard class values (at the subpixel level) in the FRM. The FRM can help to reduce the solution space of SPM and thus decrease the uncertainty in SPM and increase the subpixel resolution CD accuracy. The proposed methods provide a promising avenue for fine spatial and temporal resolution CD.

Experimental results demonstrated the five STHSPM algorithms to be effective in subpixel resolution CD, and with the information from the FRM, they can increase CD accuracy. Compared with the PSA-based subpixel resolution CD with an FRM, the proposed methods are able to achieve at least comparable CD accuracy, but need much less computing time, and hence provide new options for real-time applications. In future research, more STHSPM algorithms will be explored for subpixel resolution CD, and new ways of obtaining the required FRM will be studied.

ACKNOWLEDGMENT

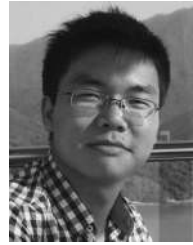
The authors would like to thank Dr. Y. Xu of The Chinese University of Hong Kong, Hong Kong, for providing the Shenzhen Landsat dataset; M. Hao of the China University of Mining and Technology, Xuzhou, China, for providing the Liaoning Landsat dataset; and Dr. X. Li and F. Ling of the

Institute of Geodesy and Geophysics, Chinese Academy of Sciences, Wuhan, China, for sharing the Brazil Landsat–MODIS dataset and codes of PSA-based CD. They would also like to thank the handling editor and anonymous reviewers whose valuable and constructive comments greatly improved this paper.

REFERENCES

- [1] D. Lu, P. Mausel, E. Brondizio, and E. Moran, “Change detection techniques,” *Int. J. Remote Sens.*, vol. 25, no. 12, pp. 2365–2407, 2004.
- [2] M. Hussain, D. Chen, A. Cheng, H. Wei, and D. Stanley, “Change detection from remotely sensed images: From pixel-based to object-based approaches,” *ISPRS J. Photogramm. Remote Sens.*, vol. 80, pp. 91–106, Jun. 2013.
- [3] A. Singh, “Digital change detection techniques using remotely-sensed data,” *Int. J. Remote Sens.*, vol. 10, no. 6, pp. 989–1003, 1989.
- [4] P. Coppin, I. Jonckheere, K. Nackaerts, and B. Muys, “Digital change detection methods in ecosystem monitoring: A review,” *Int. J. Remote Sens.*, vol. 25, no. 9, pp. 1565–1596, 2004.
- [5] L. Bruzzone and F. Bovolo, “A novel framework for the design of change-detection systems for very-high-resolution remote sensing images,” *Proc. IEEE*, vol. 101, no. 3, pp. 609–630, Mar. 2013.
- [6] F. Gao, J. Masek, M. Schwaller, and F. Hall, “On the blending of the Landsat and MODIS surface reflectance: Predicting daily Landsat surface reflectance,” *IEEE Trans. Geosci. Remote Sens.*, vol. 44, no. 8, pp. 2207–2218, Aug. 2006.
- [7] X. Zhu, J. Chen, F. Gao, X. H. Chen, and J. G. Masek, “An enhanced spatial and temporal adaptive reflectance fusion model for complex heterogeneous regions,” *Remote Sens. Environ.*, vol. 114, no. 11, pp. 2610–2623, Nov. 2010.
- [8] T. Hilker *et al.*, “A new data fusion model for high spatial- and temporal-resolution mapping of forest based on Landsat and MODIS,” *Remote Sens. Environ.*, vol. 113, no. 8, pp. 1613–1627, Aug. 2009.
- [9] B. Huang and H. Song, “Spatiotemporal reflectance fusion via sparse representation,” *IEEE Trans. Geosci. Remote Sens.*, vol. 50, no. 10, pp. 3707–3716, Oct. 2012.
- [10] H. Song and B. Huang, “Spatiotemporal satellite image fusion through one-pair image learning,” *IEEE Trans. Geosci. Remote Sens.*, vol. 51, no. 4, pp. 1883–1896, Apr. 2013.
- [11] J. M. Bioucas-Dias *et al.*, “Hyperspectral unmixing overview: Geometrical, statistical and sparse regression-based approaches,” *IEEE J. Sel. Topics Appl. Earth Observ. Remote Sens.*, vol. 5, no. 2, pp. 354–379, Apr. 2012.
- [12] D. Lu, M. Batistella, and E. Moran, “Multitemporal spectral mixture analysis for Amazonian land-cover change detection,” *Can. J. Remote Sens.*, vol. 30, no. 1, pp. 87–100, 2004.
- [13] D. Lu *et al.*, “Fractional forest cover mapping in the Brazilian Amazon with a combination of MODIS and TM images,” *Int. J. Remote Sens.*, vol. 32, no. 22, pp. 7131–7149, 2011.
- [14] V. Haertel, Y. E. Shimabukuro, and R. Almeida, “Fraction images in multitemporal change detection,” *Int. J. Remote Sens.*, vol. 25, no. 23, pp. 5473–5489, 2004.
- [15] L. O. Anderson, Y. E. Shimabukuro, and E. Arai, “Multitemporal fraction images derived from Terra MODIS data for analysing land cover change over the Amazon region,” *Int. J. Remote Sens.*, vol. 26, no. 11, pp. 2251–2257, 2005.
- [16] R. Zurita-Milla, G. Kaiser, J. G. P. W. Clevers, W. Schneider, and M. E. Schaepman, “Downscaling time series of MERIS full resolution data to monitor vegetation seasonal dynamics,” *Remote Sens. Environ.*, vol. 113, no. 9, pp. 1874–1885, Sep. 2009.
- [17] P. M. Atkinson, “Issues of uncertainty in superresolution mapping and their implications for the design of an inter-comparison study,” *Int. J. Remote Sens.*, vol. 30, no. 20, pp. 5293–5308, 2009.
- [18] P. M. Atkinson, “Downscaling in remote sensing,” *Int. J. Appl. Earth Observ. Geoinf.*, vol. 22, pp. 106–114, Jun. 2013.
- [19] K. C. Mertens, L. P. C. Verbeke, E. I. Ducheyne, and R. De Wulf, “Using genetic algorithms in sub-pixel mapping,” *Int. J. Remote Sens.*, vol. 24, no. 21, pp. 4241–4247, 2003.
- [20] Q. Wang, L. Wang, and D. Liu, “Particle swarm optimization-based sub-pixel mapping for remote-sensing imagery,” *Int. J. Remote Sens.*, vol. 33, no. 20, pp. 6480–6496, Oct. 2012.
- [21] P. M. Atkinson, “Sub-pixel target mapping from soft-classified, remotely sensed imagery,” *Photogramm. Eng. Remote Sens.*, vol. 71, no. 7, pp. 839–846, Jul. 2005.
- [22] M. W. Thornton, P. M. Atkinson, and D. A. Holland, “A linearised pixel-swapping method for mapping rural linear land cover features from fine spatial resolution remotely sensed imagery,” *Comput. Geosci.*, vol. 33, no. 10, pp. 1261–1272, Oct. 2007.
- [23] Y. Makido and A. Shortridge, “Weighting function alternatives for a sub-pixel allocation model,” *Photogramm. Eng. Remote Sens.*, vol. 73, no. 11, pp. 1233–1240, 2007.
- [24] Z. Shen, J. Qi, and K. Wang, “Modification of pixel-swapping algorithm with initialization from a sub-pixel/pixel spatial attraction model,” *Photogramm. Eng. Remote Sens.*, vol. 75, no. 5, pp. 557–567, May 2009.
- [25] A. Villa, J. Chanussot, J. A. Benediktsson, C. Jutten, and R. Dambreville, “Unsupervised methods for the classification of hyperspectral images with low spatial resolution,” *Pattern Recog.*, vol. 46, no. 6, pp. 1556–1568, Jun. 2013.
- [26] Y. Xu and B. Huang, “A spatio-temporal pixel-swapping algorithm for subpixel land cover mapping,” *IEEE Geosci. Remote Sens. Lett.*, vol. 11, no. 2, pp. 474–478, Feb. 2014.
- [27] A. J. Tatem, H. G. Lewis, P. M. Atkinson, and M. S. Nixon, “Super-resolution target identification from remotely sensed images using a Hopfield neural network,” *IEEE Trans. Geosci. Remote Sens.*, vol. 39, no. 4, pp. 781–796, Apr. 2001.
- [28] M. Q. Nguyen, P. M. Atkinson, and H. G. Lewis, “Superresolution mapping using a Hopfield neural network with fused images,” *IEEE Trans. Geosci. Remote Sens.*, vol. 44, no. 3, pp. 736–749, Mar. 2006.
- [29] A. M. Muad and G. M. Foody, “Impact of land cover patch size on the accuracy of patch area representation in HNN-based super resolution mapping,” *IEEE J. Sel. Topics Appl. Earth Observ. Remote Sens.*, vol. 5, no. 5, pp. 1418–1427, Oct. 2012.
- [30] M. Collins and M. De Jong, “Neuralizing target superresolution algorithms,” *IEEE Geosci. Remote Sens. Lett.*, vol. 1, no. 4, pp. 318–321, Oct. 2004.
- [31] X. Xu, Y. Zhong, L. Zhang, and H. Zhang, “Sub-pixel mapping based on a MAP model with multiple shifted hyperspectral imagery,” *IEEE J. Sel. Topics Appl. Earth Observ. Remote Sens.*, vol. 6, no. 2, pp. 580–593, Apr. 2013.
- [32] Q. Wang, W. Shi, and L. Wang, “Allocating classes for soft-then-hard subpixel mapping algorithms in units of class,” *IEEE Trans. Geosci. Remote Sens.*, vol. 52, no. 5, pp. 2940–2959, May 2014.
- [33] K. C. Mertens, B. D. Baset, L. P. C. Verbeke, and R. De Wulf, “A sub-pixel mapping algorithm based on sub-pixel/pixel spatial attraction models,” *Int. J. Remote Sens.*, vol. 27, no. 15, pp. 3293–3310, 2006.
- [34] X. Tong, X. Zhang, J. Shan, H. Xie, and M. Liu, “Attraction-repulsion model-based subpixel mapping of multi-/hyperspectral imagery,” *IEEE Trans. Geosci. Remote Sens.*, vol. 51, no. 5, pp. 2799–2814, May 2013.
- [35] K. C. Mertens, L. P. C. Verbeke, T. Westra, and R. De Wulf, “Sub-pixel mapping and sub-pixel sharpening using neural network predicted wavelet coefficients,” *Remote Sens. Environ.*, vol. 91, no. 2, pp. 225–236, May 2004.
- [36] Y. Gu, Y. Zhang, and J. Zhang, “Integration of spatial–spectral information for resolution enhancement in hyperspectral images,” *IEEE Trans. Geosci. Remote Sens.*, vol. 46, no. 5, pp. 1347–1358, May 2008.
- [37] D. Nigussie, R. Zurita-Milla, and J. G. P. W. Clevers, “Possibilities and limitations of artificial neural networks for subpixel mapping of land cover,” *Int. J. Remote Sens.*, vol. 32, no. 22, pp. 7203–7226, 2011.
- [38] L. Zhang, K. Wu, Y. Zhong, and P. Li, “A new sub-pixel mapping algorithm based on a BP neural network with an observation model,” *Neurocomputing*, vol. 71, no. 10–12, pp. 2046–2054, Jun. 2008.
- [39] J. Verhoeve and R. De Wulf, “Land-cover mapping at sub-pixel resolutions using linear optimization techniques,” *Remote Sens. Environ.*, vol. 79, no. 1, pp. 96–104, 2002.
- [40] A. Boucher, P. C. Kyriakidis, and C. Cronkite-Ratcliff, “Geostatistical solutions for super-resolution land cover mapping,” *IEEE Trans. Geosci. Remote Sens.*, vol. 46, no. 1, pp. 272–283, Jan. 2008.
- [41] Q. Wang, W. Shi, and L. Wang, “Indicator cokriging-based subpixel land cover mapping with shifted images,” *IEEE J. Sel. Topics Appl. Earth Observ. Remote Sens.*, vol. 7, no. 1, pp. 327–339, Jan. 2014.
- [42] H. Jin, G. Mountrakis, and P. Li, “A super-resolution mapping method using local indicator variograms,” *Int. J. Remote Sens.*, vol. 33, no. 24, pp. 7747–7773, 2012.
- [43] F. Ling *et al.*, “Interpolation-based super-resolution land cover mapping,” *Remote Sens. Lett.*, vol. 4, no. 7, pp. 629–638, 2013.
- [44] Q. Wang and W. Shi, “Utilizing multiple subpixel shifted images in subpixel mapping with image interpolation,” *IEEE Geosci. Remote Sens. Lett.*, vol. 11, no. 4, pp. 798–802, Apr. 2014.
- [45] G. M. Foody, A. M. Muslim, and P. M. Atkinson, “Super-resolution mapping of the waterline from remotely sensed data,” *Int. J. Remote Sens.*, vol. 26, no. 24, pp. 5381–5392, 2005.

- [46] Y. F. Su, G. M. Foody, A. M. Muad, and K. S. Cheng, "Combining Hopfield neural network and contouring methods to enhance super-resolution mapping," *IEEE J. Sel. Topics Appl. Earth Observ. Remote Sens.*, vol. 5, no. 5, pp. 1403–1417, Oct. 2012.
- [47] Y. Ge, S. Li, and V. C. Lakhan, "Development and testing of a subpixel mapping algorithm," *IEEE Trans. Geosci. Remote Sens.*, vol. 47, no. 7, pp. 2155–2164, Jul. 2009.
- [48] T. Kasetkasem, M. K. Arora, and P. K. Varshney, "Super-resolution land-cover mapping using a Markov random field based approach," *Remote Sens. Environ.*, vol. 96, no. 3/4, pp. 302–314, Jun. 2005.
- [49] V. A. Tolpekin and A. Stein, "Quantification of the effects of land-cover-class spectral separability on the accuracy of Markov-random-field based superresolution mapping," *IEEE Trans. Geosci. Remote Sens.*, vol. 47, no. 9, pp. 3283–3297, Sep. 2009.
- [50] J. P. Ardila, V. A. Tolpekin, W. Bijker, and A. Stein, "Markov-random-field-based super-resolution mapping for identification of urban trees in VHR images," *ISPRS J. Photogramm. Remote Sens.*, vol. 66, no. 6, pp. 762–775, Nov. 2011.
- [51] X. Li, F. Ling, Y. Du, and Y. Zhang, "Spatially adaptive superresolution land cover mapping with multispectral and panchromatic images," *IEEE Trans. Geosci. Remote Sens.*, vol. 52, no. 5, pp. 2810–2823, May 2014.
- [52] G. M. Foody and H. T. X. Doan, "Variability in soft classification prediction and its implications for sub-pixel resolution change detection and super-resolution mapping," *Photogramm. Eng. Remote Sens.*, vol. 73, no. 8, pp. 923–933, 2007.
- [53] F. Ling, W. Li, Y. Du, and X. Li, "Land cover change mapping at the subpixel scale with different spatial-resolution remotely sensed imagery," *IEEE Geosci. Remote Sens. Lett.*, vol. 8, no. 1, pp. 182–186, Jan. 2011.
- [54] X. Li, Y. Du, and F. Ling, "Super-resolution mapping of forests with bitemporal different spatial resolution images based on the spatial-temporal Markov random field," *IEEE J. Sel. Topics Appl. Earth Observ. Remote Sens.*, vol. 7, no. 1, pp. 29–39, Jan. 2014.
- [55] Q. Wang, W. Shi, and P. M. Atkinson, "Sub-pixel mapping of remote sensing images based on radial basis function interpolation," *ISPRS J. Photogramm. Remote Sens.*, vol. 92, pp. 1–15, Jun. 2014.
- [56] A. M. Muad and G. M. Foody, "Super-resolution mapping of lakes from imagery with a coarse spatial and fine temporal resolution," *Int. J. Appl. Earth Observ. Geoinf.*, vol. 15, pp. 79–91, Apr. 2012.
- [57] F. Ling, Y. Du, F. Xiao, H. Xue, and S. Wu, "Super-resolution land-cover mapping using multiple sub-pixel shifted remotely sensed images," *Int. J. Remote Sens.*, vol. 31, no. 19, pp. 5023–5040, Jun. 2010.
- [58] L. Wang and Q. Wang, "Subpixel mapping using Markov random field with multiple spectral constraints from subpixel shifted remote sensing images," *IEEE Geosci. Remote Sens. Lett.*, vol. 10, no. 3, pp. 598–602, May 2013.
- [59] P. Goovaerts, *Geostatistics for Natural Resources Evaluation*. London, U.K.: Oxford Univ. Press, 1997.
- [60] M. Hao, W. Shi, H. Zhang, and C. Li, "Unsupervised change detection with expectation-maximization-based level set," *IEEE Geosci. Remote Sens. Lett.*, vol. 11, no. 1, pp. 210–214, Jan. 2014.
- [61] L. Wang, D. Liu, and Q. Wang, "Geometric method of fully constrained least squares linear spectral mixture analysis," *IEEE Trans. Geosci. Remote Sens.*, vol. 51, no. 6, pp. 3558–3566, Jun. 2013.
- [62] P. Fisher, "The pixel: A snare and a delusion," *Int. J. Remote Sens.*, vol. 18, no. 3, pp. 679–685, 1997.
- [63] P. M. Atkinson, "Resolution manipulation and sub-pixel mapping," in *Remote Sensing Image Analysis: Including the Spatial Domain*, S. M. de Jong and F. D. van der Meer, Eds. Dordrecht, The Netherlands: Kluwer, 2006, pp. 51–70.
- [64] Q. Wang, P. M. Atkinson, and W. Shi, "Indicator cokriging-based subpixel mapping without prior spatial structure information," *IEEE Trans. Geosci. Remote Sens.*, vol. 53, no. 1, pp. 309–323, Jan. 2015.
- [65] P. Aplin and P. M. Atkinson, "Sub-pixel land cover mapping for per-field classification," *Int. J. Remote Sens.*, vol. 22, no. 14, pp. 2853–2858, 2001.
- [66] Z. Mahmood, M. A. Akhter, G. Thoonen, and P. Scheunders, "Contextual subpixel mapping of hyperspectral images making use of a high resolution color image," *IEEE J. Sel. Topics Appl. Earth Observ. Remote Sens.*, vol. 6, no. 2, pp. 779–791, Apr. 2013.
- [67] A. Robin, S. Le Hegarat-Masclé, and L. Moisan, "Unsupervised sub-pixel classification using coarse-resolution time series and structural information," *IEEE Trans. Geosci. Remote Sens.*, vol. 46, no. 5, pp. 1359–1374, May 2008.



Qunming Wang received the B.S. and M.S. degrees from Harbin Engineering University, Harbin, China, in 2010 and 2012, respectively. He is currently working toward the Ph.D. degree in the Department of Land Surveying and Geo-Informatics, The Hong Kong Polytechnic University, Kowloon, Hong Kong.

From June to December 2013, he was a Visiting Ph.D. Student in Geography and Environment, University of Southampton, Southampton, U.K. His current research interests focus on remote sensing

image analysis, pattern recognition, and geostatistics.

Mr. Wang serves as a Reviewer for over ten international journals, including the IEEE TRANSACTIONS ON GEOSCIENCE AND REMOTE SENSING, the IEEE TRANSACTIONS ON CYBERNETICS, the IEEE GEOSCIENCE AND REMOTE SENSING LETTERS, the IEEE JOURNAL OF SELECTED TOPICS IN APPLIED EARTH OBSERVATION AND REMOTE SENSING, PHOTOGRAMMETRIC ENGINEERING AND REMOTE SENSING, the INTERNATIONAL JOURNAL OF REMOTE SENSING, and REMOTE SENSING LETTERS. He was the recipient of the Excellent Master Dissertation Award and the Excellent Graduates in Heilongjiang Province, China, in 2012. He has been also a recipient of the hypercompetitive Hong Kong Ph.D. Fellowship.



Peter M. Atkinson received the B.Sc. degree in geography from The University of Nottingham, Nottingham, U.K., in 1986, the Ph.D. degree from The University of Sheffield (NERC CASE award with Rothamsted Experimental Station), Sheffield, U.K., in 1990, and the MBA degree from the University of Southampton, Southampton, U.K., in 2012.

He is currently a Professor of geography with the University of Southampton. He has authored or coauthored over 170 peer-reviewed articles in international scientific journals and around 50 refereed

book chapters. He has also edited nine journal special issues and eight books. His research focus is in remote sensing, geographical information science, and spatial (and space-time) statistics applied to a range of environmental science and socioeconomic problems.

Prof. Atkinson sits on various international scientific committees. He has organized several major international conferences in Southampton, including GeoComputation in 2003 and GeoENV in 2008. He is an Associate Editor of *Computers and Geosciences* and sits on the editorial boards of several other journals, including *Geographical Analysis*, *Spatial Statistics*, the *International Journal of Applied Earth Observation and Geoinformation*, and *Environmental Informatics*.



Wenzhong Shi received the Ph.D. degree from the University of Osnabrück, Vechta, Germany, in 1994.

He is currently a Chair Professor in geographical information science (GIS) and remote sensing, Department of Land Surveying and Geo-Informatics, The Hong Kong Polytechnic University, Kowloon, Hong Kong. He is also currently with Wuhan University, Wuhan, China. He has authored or coauthored over 100 SCI papers and ten books. His current research interests include GIS and remote sensing, uncertainty and spatial data quality control, and image

processing for high-resolution satellite images.

Prof. Shi was a recipient of the State Natural Science Award from the State Council of China in 2007 and The Wang Zhizhuo Award from the International Society for Photogrammetry and Remote Sensing in 2012.